

# New insights of natural fractures growth and stimulation optimization based on a three-dimensional cohesive zone model

Chuang Liu<sup>a</sup>, JiaNing Zhang<sup>a</sup>, Hao Yu<sup>a</sup>, Jie Chen<sup>b</sup>, DeTang Lu<sup>a</sup>, HengAn Wu<sup>a,\*</sup>

<sup>a</sup> CAS Key Laboratory of Mechanical Behavior and Design of Materials, Department of Modern Mechanics, University of Science and Technology of China, Hefei, 230027, Anhui, PR China

<sup>b</sup> Zhongtian Technologies Submarine Cable Co., Ltd, Jiangsu Nantong, No.1 Xinkai South Road, PR China

## ARTICLE INFO

### Keywords:

Hydraulic fracturing  
Numerical simulation  
Cohesive element  
Fractures intersection  
Natural fracture

## ABSTRACT

A fully coupled fluid-solid three-dimensional model based on cohesive zone method is presented to simulate the interactions between hydraulic fracture (HF) and natural fracture (NF). Unknown interaction mechanisms of the crossing, arresting and bypassing are revealed. The interactions between HF and NF in three dimensions are shown to be more complex than in two dimensions. Numerical results demonstrate that vertical stress contrast plays a significant effect on the fracture geometry for single and multiple stages fracturing treatments. Multiple fractures propagation of different fracturing sequences under the influence of NFs distribution and in-situ stresses is investigated. For Texas-two step fracturing method, the propagation of interior HF in horizontal direction will be terminated by stress perturbation in closely spaced HF. A method to weaken severe mechanical interactions and enlarge the separations of NFs is proposed. The findings provide some new insights for stimulation design to create fracture network.

## 1. Introduction

Hydraulic fracturing treatments have been widely applied in unconventional reservoirs development to enhance formation permeability. The pre-existing NFs are recognized as one of the principle mechanisms effecting the propagation trajectories of the hydraulically driven fractures. The successfully development of unconventional reservoirs relies on the stimulation technique to reopen the cemented NFs and create fracture network. The NFs are distributed randomly in the reservoirs (Gale et al., 2014). Due to the complex in-situ conditions and multiple couplings, acquiring the interaction mechanisms between HF and NFs is still a challenge work. Renshaw and Pollard (1995) developed a criterion to predict whether a hydraulic fracture will cross an orthogonal natural fracture. The criterion is based on the stress solution of linear elasticity fracture mechanics. And it is extended to the conditions of nonorthogonal intersection by Gu and Weng (2010). Chuprakov et al. (2014) developed an OpenT model that takes into account the mechanical influence of the HF opening and the permeability of the NF with an assumption of uniform pressure distribution in NF surfaces. Due to the complexity of fluid-solid coupling of the fractures intersection, the analytical models based on several simplifications do not take into account the coupled fluid flow and the nonuniform stress distribution

acting on the NF surfaces. Numerical models have been developed to study the complex interactions between fractures. The finite element models based on cohesive zone method are adopted to investigate a HF interacting with a NF (Chen et al., 2017; Guo et al., 2015). The effect of approaching angle, in-situ stresses and fluid viscosity are studied. They found that HF will cross NF under the conditions of low horizontal in-situ stress contrast and high approaching angle. The displacement discontinuity method (DDM) is applied to simulate fractures interaction problems (Behnia et al., 2015; Zhang et al., 2007; Zhang and Jeffrey, 2014, 2006). The method is extended to pseudo three-dimensions to account for nonuniform distribution of fractures aperture in vertical direction (Kresse et al., 2013; Weng et al., 2014). Recently, the extended finite element method (XFEM) and phase field method are developed to simulate fractures intersection without remeshing (Guo et al., 2018; Shi et al., 2017; Wang et al., 2018). Due to the complexity in building enrichments for strong discontinuities and convergence difficulties, the simulation of fractures intersection based on XFEM in three dimensions is still a challenge work. The previous studies assume the vertical extents of HF and NF are identical to reduce the dimensionality of the problem to two dimensions. The intersections between HF and NF are classified to be three modes based on the plane strain assumption: HF propagating along NF, HF crossing NF and NF staying closed, HF crossing NF with the

\* Corresponding author.

E-mail address: [wuha@ustc.edu.cn](mailto:wuha@ustc.edu.cn) (H. Wu).

<https://doi.org/10.1016/j.jngse.2020.103165>

Received 14 July 2019; Received in revised form 31 December 2019; Accepted 12 January 2020

Available online 22 January 2020

1875-5100/© 2020 Elsevier B.V. All rights reserved.

slippage of NF (Gu et al., 2012). However, the assumption limits the intersection modes between HF and NF.

Experimental observations have demonstrated conditions in which a HF is diverted into a NF and a HF bypasses a NF with the separation of bonded interfaces and a HF bypasses a NF and diverts down it to form separate fractures (Bahorich et al., 2012). The complex geometries of fractures intersection are mainly attributed to the different vertical extents of HF and NF. Recently, researchers focus on the development of three-dimensional numerical models to capture the complex interactions between HFs and NFs. A fully coupled hydromechanical discrete-fracture networks (DFN) model to simulate fluid flowing and proppant transporting within predefined paths is developed (McClure et al., 2016; Shiozawa and McClure, 2016). A DDM-based three-dimensional model is presented demonstrating the partial failure of NF induced by the approaching HF (Shrivastava et al., 2018). Yoshioka and Bourdin (2016) developed a fracture intersection model based on phase field method. Settgaest et al. (2017) established a fully coupled three-dimensional model for massively parallel simulation of HFs under the influence of NFs.

The three-dimensional models posed above provide more details about fractures intersections. In the current work, we aim to investigate the effect of heterogeneity of rock on the fracture geometry, and find out the controlling factors affecting the fractures intersection modes such as the crossing, diverting and bypassing in three dimensions. Due to the advantages of computational expense and convergence efficiency, the two-dimensional models are still widely used in engineering. Therefore, we try to find out the applicable conditions of the plain strain models. In addition, optimal designs to enlarge the separations of NF is studied.

## 2. Model and numerical method

The cohesive zone method is used in this paper to simulate the discontinuities introduced by the fractures through traction-separation law. The method regards fracture as a gradual phenomenon in which separation takes place across an extended crack 'tip', or cohesive zone, and is resisted by cohesive tractions (Ortiz and Pandolfi, 1999). The cohesive elements are placed between bulk elements to describe the cohesive forces which occur when material elements are being pulled apart. The manuscript has been revised accordingly.

### 2.1. Traction-separation law

The predefined cohesive elements based on traction-separation law are used to simulate the initiation and propagation of HFs and NFs. The traction-separation model assumes initially linear elastic behavior followed by the initiation and evolution of damage. The constitutive behavior relates the nominal stresses to the nominal strains across the interface. Damage initiation represents the beginning of degradation of the material. Due to the complexity of in-situ conditions, the opening of fractures often exhibited mixed fracture modes. Therefore, the effect of normal and shear tractions on fracture initiation must be considered. Quadratic nominal stress criterion is adopted in this paper due to it has been widely used in determining fracture initiation of mixed fracture modes (Sun et al., 2019). The criterion defines that damage is initiated when a quadratic function involving the nominal stress ratios reaches a value of one. The criterion is written as

$$\left\langle \frac{t_n}{t_n^0} \right\rangle^2 + \left\langle \frac{t_s}{t_s^0} \right\rangle^2 + \left\langle \frac{t_t}{t_t^0} \right\rangle^2 = 1 \quad (1)$$

where  $t_n$ ,  $t_s$  and  $t_t$  represent the nominal and the two shear tractions, respectively.  $t_n^0$ ,  $t_s^0$  and  $t_t^0$  represent the peak values of nominal stress. The symbol  $\langle \cdot \rangle$  is the Macaulay bracket, which means a pure compressive deformation does not initiate damage. The nominal stresses in the above equation are calculated based on the linear elastic constitutive relation defined in traction-separation law. The elastic parameters are provided

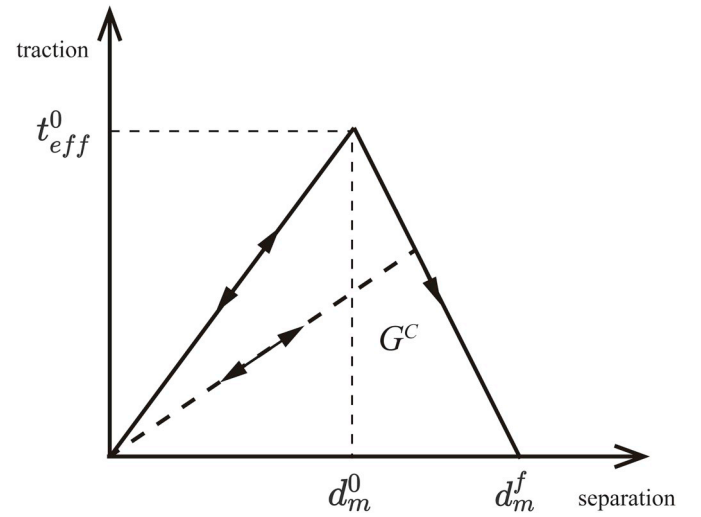


Fig. 1. Bilinear traction-separation law.

by the materials of cohesive elements. The opening of cohesive elements is calculated through solving system equilibrium equations. A nondimensional variable  $D$  denotes the overall damage of the material. It is equal to 0 initially, and monotonically increases from 0 to 1 after the damage initiation. The traction components are given as follows

$$t = \begin{cases} (1-D)\bar{t}, & \text{damage occurs} \\ \bar{t}, & \text{without damage} \end{cases} \quad (2)$$

where  $t = \{t_n, t_s, t_t\}$  is the nominal traction stress vector,  $\bar{t} = \{\bar{t}_n, \bar{t}_s, \bar{t}_t\}$  is the stress tensor predicted for the current strains without damage.

The damage evolution is described by the fracture energy. For the mixed fracture modes, the total fracture energy is composed of the work induced by the tractions along normal and two shear directions. The Benzeggagh-Kenane fracture criterion (BK) is used as we assume the critical fracture energies during deformation purely along two shear directions are the same (Benzeggagh and Kenane, 1996). The first component involves specifying the energy dissipated due to failure,  $G_C$ . The fracture energy is defined to be the function of mode mix of the deformation field. It is given as follows

$$G_n^C + (G_s^C - G_n^C) \left\{ \frac{G_s}{G_T} \right\}^\eta = G_C \quad (3)$$

where  $G_s$  is the work done by the shear directions, and  $G_T$  is the total work.  $G_s/G_T$  denotes the proportions of the work done by shear traction,  $G_n^C$  and  $G_s^C$  refer to the critical fracture energies required to cause failure in the normal and shear directions, respectively,  $\eta$  is a scalar material parameter.  $G_s/G_T$  defined in the Benzeggagh-Kenane criterion can be used to characterize the deformations purely along normal and shear directions (i.e. as the fracture deforms along shear directions,  $G_s/G_T = 1$ , and as the fracture deforms along normal direction,  $G_s/G_T = 0$ ). The second component to be defined is the nature of the evolution of damage variable,  $D$ . A bilinear-damage evolution law is used in this paper as shown in Fig. 1. The damage variable  $D$ , is written as (Abaqus 6.14)

$$D = \frac{d_m^f (d_m^{\max} - d_m^0)}{d_m^{\max} (d_m^f - d_m^0)} \quad (4)$$

where  $d_m^0$ ,  $d_m^f = 2G^C/t_{eff}^0$  represent the effective displacement at damage initiation and complete failure, respectively,  $t_{eff}^0$  is the effective traction at damage initiation,  $d_m^{\max}$  is the maximum value of the effective displacement during the loading history. The effective value of variables such as effective displacement and traction,  $\delta_m$ , is defined as  $\delta_m =$

$\sqrt{\delta_n^2 + \delta_s^2 + \delta_t^2}$ . Where  $\delta_n$ ,  $\delta_s$  and  $\delta_t$  are the values of displacement or traction along normal and shear directions, respectively.  $t_{eff}^0$  and  $d_m^0$  are constant calculated from the parameters of the material of cohesive element.  $d_m^f$  is varying with the quantity of mode mix  $G_S/G_T$  during fracture propagation.

## 2.2. Fluid flow within fractures

The fluid flow is consisting of tangential flow within the fracture surfaces, fluid leakoff which represents fluid flow across fracture surfaces, and fluid flow in porous media. The fluid is assumed to be incompressible. The tangential flow along fracture surfaces is governed by the lubrication equation (Batchelor and Batchelor, 2000).

$$\mathbf{q} = -\frac{w^3}{12\mu} \nabla p_f \quad (5)$$

The mass conservation equation is written as

$$\frac{\partial w}{\partial t} + \nabla \cdot \mathbf{q} + q_t + q_b = Q(t)\delta(\mathbf{x}) \quad (6)$$

where  $p_f$  is the fluid pressure within the fracture,  $w$  is the fracture aperture,  $\mu$  is the fluid viscosity,  $\mathbf{q}$  is the fluid flux of the tangential flow,  $q_t$  and  $q_b$  are the rates of fluid leakoff into the adjacent rocks,  $Q(t)$  is the injection rate, and  $\delta(\cdot)$  is the Dirac delta function. The rate of fluid leakoff is written defined as (Abaqus 6.14)

$$\begin{cases} q_t = c_t(p_f - p_t) \\ q_b = c_b(p_f - p_b) \end{cases} \quad (7)$$

where  $p_t$  and  $p_b$  are pore pressure in the adjacent rock matrix,  $c_t$  and  $c_b$  are the corresponding fluid leakoff coefficients. Substituting Eq. (5) and Eq. (7) to Eq. (6) yields the equation

$$\frac{\partial w}{\partial t} - \frac{1}{12\mu} \nabla \cdot (w^3 \nabla p_f) + c_t(p_f - p_t) + c_b(p_f - p_b) = Q(t)\delta(\mathbf{x}) \quad (8)$$

## 2.3. Fluid flow in porous media

The mass conservation equation of the fluid flow in porous media can be written as

$$\varphi \frac{\partial \rho_f}{\partial t} + \nabla \cdot (\rho_f \mathbf{v}) = 0 \quad (9)$$

where  $\rho_f$  is the density of the fluid in the rock matrix,  $\varphi$  is the porosity of rock and  $\mathbf{v}$  is the seepage velocity. Darcy's law presents the relation between seepage velocity and the fluid porous pressure

$$\mathbf{v} = -\frac{\kappa}{\mu} \nabla p_m \quad (10)$$

where the permeability  $\kappa$  is a second-order tensor, for the case of isotropic medium, the permeability is a scalar,  $\mu$  is the dynamic viscosity of the fluid,  $p_m$  is pore pressure of the porous medium. Substituting Eq. (10) to Eq. (9) yields

$$\varphi \frac{\partial \rho_f}{\partial t} - \nabla \cdot \left( \rho_f \frac{\kappa}{\mu} \nabla p_m \right) = 0 \quad (11)$$

## 2.4. Discretization of the governing equations

The equilibrium equation in fluid filled porous media can be written in terms of the effective stress  $\boldsymbol{\sigma}'$

$$\nabla \cdot (\boldsymbol{\sigma}' + p_m \mathbf{I}) = 0 \quad (12)$$

By introducing the test function  $\delta \mathbf{u}(\mathbf{x})$  for the displacement field, the

weak form of the equilibrium equation can be written as

$$\int_{\Omega_u} \delta \boldsymbol{\varepsilon} : \boldsymbol{\sigma} d\Omega - \int_{\Omega_u} \delta \mathbf{u} \cdot \nabla p_m d\Omega - \int_{\Gamma} \mathbf{t}_i \cdot \delta \mathbf{u} d\Gamma = 0 \quad (13)$$

where  $\Omega_u$  is the region of displacement field. The leakoff term in Eq. (8) is the flux boundary condition. The leakoff coefficients of the opposite fracture surfaces are assumed to be the same ( $c_t = c_b = c_f(\mathbf{x})$ ). The fracture permeability  $k$  is defined as  $k = \frac{w^3}{12\mu}$ . By introducing the test function  $\delta p_f(\mathbf{x})$  for fluid pressure within fractures, the weak form of Eq. (8) can be obtained

$$\begin{aligned} & \int_{\Omega_f} \delta p_f \frac{\partial w}{\partial t} d\Omega + \int_{\Omega_f} k \delta \nabla p_f \cdot \nabla p_f d\Omega \\ & - \int_{\Gamma} \delta p_f c_f (p_f - p_m) d\Gamma - \delta p_f Q(t)|_{\mathbf{x}=\mathbf{x}_0} = 0 \end{aligned} \quad (14)$$

where  $\Omega_f$  is the region within fracture;  $\Gamma$  is the region of fracture surfaces;  $\mathbf{x}_0$  is the position of injection point.

We assume the density of fluid and permeability are constant in porous media. By introducing the test function  $\delta p_m$  for pore pressure of porous media, the weak form of Eq. (11) is written as

$$\int_{\Omega_m} \delta \nabla p_m \cdot \frac{\kappa}{\mu} \nabla p_m d\Omega - \int_{\Gamma} \delta p_m c_f (p_m - p_f) d\Gamma = 0 \quad (15)$$

where  $\Omega_m$  is the region of rock matrix. The displacement  $\mathbf{u}(\mathbf{x}, t)$ , fluid pressure within fractures  $p_f(\mathbf{x}, t)$ , pore pressure in rocks  $p_m(\mathbf{x}, t)$ , and fracture aperture  $w(\mathbf{x}, t)$  can be approximated by the shape functions as

$$\mathbf{u}(\mathbf{x}, t) = \sum_{I \in N_u} N_I^u \mathbf{u}_I(t) \quad (16)$$

$$p_f(\mathbf{x}, t) = \sum_{I \in N_f} N_I^f p_f(t) \quad (17)$$

$$p_m(\mathbf{x}, t) = \sum_{I \in N_m} N_I^m p_m(t) \quad (18)$$

$$w(\mathbf{x}, t) = \sum_{I \in N_w} N_I^w \mathbf{u}_I = \mathbf{N}^w \mathbf{U} \quad (19)$$

where  $N_u$ ,  $N_f$  and  $N_m$  are the node set of displacement, fluid nodes within fractures, and pore pressure, respectively;  $N_I^u$ ,  $N_I^f$  and  $N_I^m$  are the shape function of displacement, fluid nodes within fractures, and pore pressure, respectively;  $N_I^w$  is the shape function which transfers the node displacement to fracture aperture;  $\mathbf{U}$  is the node displacement vector.

Substituting the approximations of the displacement, fluid pressure and pore pressure (Eq. (16) – (19)) into the weak form of the governing equations (Eq. (13) – (15)), the nonlinear coupled equations can be discretized as

$$\mathbf{K} \mathbf{U} + \mathbf{Q} \mathbf{P}_m - \mathbf{F}^{ext} = 0 \quad (20)$$

$$\mathbf{M} \dot{\mathbf{U}} + \mathbf{H} \mathbf{P}_f + \mathbf{R} \mathbf{P}_m + \mathbf{S} = 0 \quad (21)$$

$$\mathbf{L} \mathbf{P}_m - \mathbf{N} \mathbf{P}_f = 0 \quad (22)$$

In Eq. (20),  $\mathbf{K}$ ,  $\mathbf{Q}$  and  $\mathbf{F}^{ext}$  are written as

$$\mathbf{K} = \int_{\Omega_u} \mathbf{B}^T \mathbf{D} \mathbf{B} d\Omega \quad (23)$$

$$\mathbf{Q} = \int_{\Omega_u} (\mathbf{N}^u)^T (\nabla \mathbf{N}^m) d\Omega \quad (24)$$

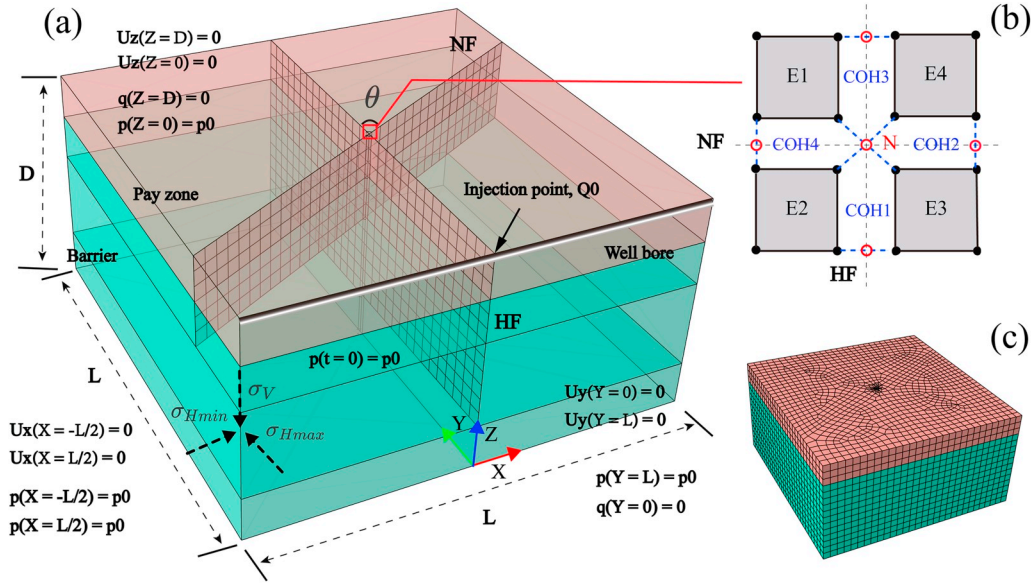


Fig. 2. Schematically representation of the fractures intersection model, (a) the position of predefined NF and HF, (b) connection of cohesive element at the intersection point, (c) mesh scheme of the numerical model.

$$\mathbf{F}^{ext} = \int_{\Gamma} (\mathbf{N}^u)^T \mathbf{t} d\Gamma \quad (25)$$

where  $\mathbf{B}$  is the matrix of displacement shape function derivatives;  $\mathbf{D}$  is the elastic constitutive matrix;  $\mathbf{P}_m$  is the vector of pore pressure;  $\mathbf{F}^{ext}$  is the external loading vector; the traction  $\mathbf{t}$  is the function of  $p_f$ , and it can be expressed as  $\mathbf{t} = \int_{\Gamma} \mathbf{N}^p p_f d\Gamma$ .

In Eq. (21), the  $\mathbf{H}$  is expressed in terms of the displacement  $\mathbf{U}$ , and the source term  $\mathbf{S}$  are written as

$$\mathbf{M} = \int_{\Omega_f} (\mathbf{N}^f)^T (\mathbf{N}^w) d\Omega \quad (26)$$

$$\mathbf{H} = - \int_{\Gamma} (\mathbf{N}^f)^T c_f \mathbf{N}^f d\Gamma + \int_{\Omega_f} k (\nabla \mathbf{N}^f)^T \nabla \mathbf{N}^f d\Omega \quad (27)$$

$$\mathbf{R} = \int_{\Gamma} (\mathbf{N}^f)^T c_f \mathbf{N}^m d\Gamma \quad (28)$$

$$\mathbf{S} = \mathbf{N}^f \mathbf{Q}(t)|_{x=x_0} \quad (29)$$

In Eq. (22),  $\mathbf{L}$  and  $\mathbf{N}$  are written as

$$\mathbf{L} = \int_{\Omega_m} (\nabla \mathbf{N}^m)^T \frac{\mathbf{K}}{\mu} (\nabla \mathbf{N}^m) d\Omega - \int_{\Gamma} (\mathbf{N}^m)^T c_f \mathbf{N}^m d\Gamma \quad (30)$$

$$\mathbf{N} = \int_{\Gamma} (\mathbf{N}^m)^T c_f \mathbf{N}^f d\Gamma \quad (31)$$

The implicit integration method is applied to the time discretization of Eq. (20) – (22). The coupled discretized system equations are solved by the Newton-Raphson interactive method.

## 2.5. Numerical implementation

The commercial finite element software ABAQUS is used to solve the coupled equations posed above. The 8-nodes (C3D8P) solid element and 8-nodes displacement with 4-nodes pore pressure cohesive element (COH3D8P) are adopted to model the rock matrix and the fractures,

respectively. Fig. 2 shows the scheme of the predefined cohesive elements path of HF connected to the path of NF. Due to the symmetry of the problem, a quarter of the model is considered. The initiation and propagation of HF starts from the wellbore which is orientated parallel to the minimum horizontal in-situ stress,  $\sigma_{Hmin}$ . The vertical oriented NF is put within pay zone and barrier at the angle,  $\theta$ . The  $\theta$  is defined to be the acute angle of the intersection angles. Fig. 2b shows the top view of single layer elements at the intersection point. The separated solid elements (E1, E2, E3, E4) are connected by the cohesive elements (COH1, COH2, COH3, COH4). The fluid pressure within the fractures is characterized by the middle nodes of the cohesive elements. The middle nodes of different cohesive elements at the intersection point are combined together to make the pressure continuity condition as shown in Fig. 2b, which enables the penetration of hydraulic fluid into different fracture branches. The boundary and initial conditions are described by the equations, i.e.  $U_x(X = -L/2) = 0$  implies the displacement of x-components at the boundary surface defined by the norm vector ( $X = -L/2$ ) is zero.  $p$  is defined as the pore pressure and  $q$  is the fluid velocity.

## 2.6. Model verification

### 2.6.1. Comparing with penny-shaped analytical solution

In this section, we verify the model by the asymptotic solutions of penny-shaped fluid-driven fracture proposed by Savitski and Detournay (2002). The analytical solution depends only on one parameter, which can be selected as the dimensionless toughness,  $\mathcal{K}$ . The propagation of hydraulic fracture is classified to be the viscosity-dominated regime ( $\mathcal{K} \leq 1$ ), the mixed-regime ( $1 < \mathcal{K} < 3.5$ ), and the toughness-dominated regime ( $\mathcal{K} \geq 3.5$ ). The dimensionless toughness is defined as

$$\mathcal{K} = K' \left( \frac{t^2}{\mu'^3 Q_0^3 E'^3} \right)^{1/18} \quad (32)$$

where  $\mu' = 12\mu$ ;  $K' = 4(2/\pi)^{1/2} K_{IC}$ ;  $E' = E/(1 - \nu^2)$ ;  $K_{IC}$  is the critical fracture toughness;  $Q_0$  is the injection rate.

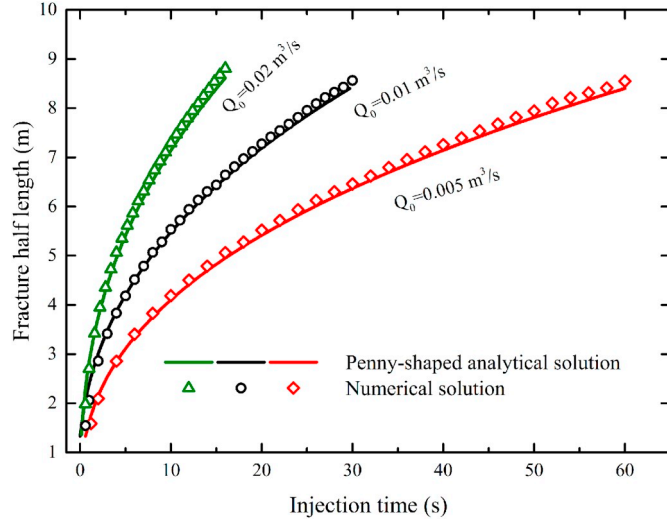
In this section, only the propagation of toughness-dominated regime is considered for discussion. The solution of fracture radius of toughness-dominated regime is written as



**Table 1**

Input parameters of the verification cases.

Parameters	Value	Units
Elastic modulus $E$	20	GPa
Poisson's ratio $\nu$	0.2	–
Fracture toughness $K_{IC}$	6.45	MPa·m <sup>1/2</sup>
Injection rate $Q_0$	0.005, 0.01, 0.02	m <sup>3</sup> /s
Viscosity $\mu$	0.001	Pa·s

**Fig. 3.** Comparison between the numerical model and the penny-shaped analytical solution in terms of fracture growth rate.

$$R(t) = \left( \frac{Q_0^2 E^2 t^2}{K^2} \right)^{1/5} (0.8546 - 0.7349 \mathcal{M}) \quad (33)$$

where  $\mathcal{M} = \mathcal{H}^{-18/5}$ .

The numerical model is built based on the plain strain assumption due to the axis symmetry of the problem. The size of the model is 20 m × 20 m. Three cases of injection rates are presented for the simulations ( $Q_0 = 0.005 \text{ m}^3/\text{s}$ ,  $0.01 \text{ m}^3/\text{s}$ ,  $0.02 \text{ m}^3/\text{s}$ ). Details of input parameters are listed in Table 1. According to Eq. (31),  $\mathcal{H}$  decreases with the injection rate  $Q_0$ , and increases with the injection time  $t$ . Therefore,  $\mathcal{H}$  for the case of higher injection rate ( $Q_0 = 0.02 \text{ m}^3/\text{s}$ ) is less than the other cases. In addition, the solution is viscosity-dominated regime initially ( $\mathcal{H} = 0$  at  $t = 0$ ), and evolves to toughness-dominated eventually. To avoid the regime shifting, the solutions at very early injection stages are neglected in the verification.  $\mathcal{H}$  for the injection rate  $Q_0 = 0.02 \text{ m}^3/\text{s}$  at the injection time  $t = 0.5 \text{ s}$  is equal to 4.414. Therefore, the propagation of the fractures in the three cases is toughness-dominated regime ( $\mathcal{H} > 3.5$ ) as  $t \geq 0.5 \text{ s}$ . Fig. 3 shows the growth of fracture half length of different injection rates. The numerical results match the analytical solutions well.

### 2.6.2. Comparing with experiment results

We present two simulation cases of fractures intersection comparing with the experimental results of Bahorich et al. (2012). In the experiment, a wellbore was placed in the central area of test block. Natural fractures were placed near the wellbore either orthogonal or oblique to the direction of the maximum horizontal stress to ensure hydraulic fracture/natural fracture intersection. Two rubber flat jacks inside of an aluminum box were used to apply horizontal stresses. Another flat jack was placed between the block and an apparatus lid to apply the vertical stress. The flat jack was fixed after applying stresses to the block. And fluid was injected into the wellbore to initiate a fracture. The simulation

**Table 2**

Input parameters of the model.

Parameters	Values	Unit
Dimensions of the model	$1 \times 1 \times 0.5$	foot
Elastic of gypsum plaster	200,000	psi
Elastic of hydrostone	250,000	psi
Tensile strength of gypsum plaster	300	psi
Tensile strength of hydrostone	700	psi
Permeability of gypsum plaster	57.3	mD
Permeability of hydrostone	7.2	mD
Vertical in-situ stress	100	psi
Maximum horizontal in-situ stress	75	psi
Minimum horizontal in-situ stress for shorter NF case	60	psi
Minimum horizontal in-situ stress for taller NF case	25	psi
Fluid viscosity	118	cp

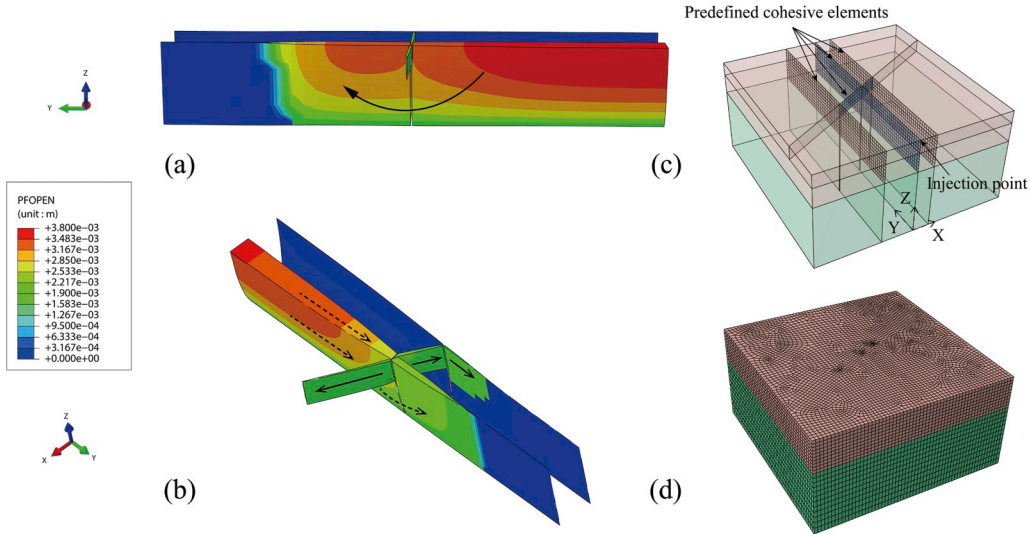
parameters are selected from the experiment settings. The main differences of the two simulation cases are the size and orientation of NF and the horizontal stress contrast. The shorter NF is 1 in tall and 3 in long, and the taller one is 1.55 in tall and 3 in long. The intersection angle  $\theta$  for the cases of shorter and taller NF is  $90^\circ$  and  $60^\circ$ , respectively. The dimensions of the experiments are one-foot cubes. There are three layers in the cubes, the top and bottom layers are hydrostone and the middle layer is gypsum plaster. The top and bottom layers provide a vertical containment which implies the restrictions of fractures propagation along vertical direction so that the HF will propagate within middle layer. NF is put in the middle of gypsum plaster layer. Due to the symmetry of the problem, only a half of model is considered in the simulations. Table 2 provides the detail input parameters of the verification cases.

Fig. 4a shows the fracture trajectories for the case of shorter NF. The HF bypass NF in conjunction with a separation of NF without additional propagation beyond the NF tips, which is coincident with the geometry observed in the experiment (ref. Fig. 15 of Bahorich et al., 2012). Fig. 4b shows the fracture propagation paths for the case of taller NF. The HF is bypassing the NF with interfacial separation and fluid intrusion along the NF. The branched fracture continues propagating in one side of the NF tip (A) and terminated in the other side (B). The laboratory experiment observed similar geometries of fractures for the case of taller NF (ref. Fig. 17 of Bahorich et al., 2012). The exactly matched results verify the accuracy of the presented model in modelling fractures intersection.

## 3. Simulation results and discussion

### 3.1. Sensitivity to intersection angle

The intersection angle between hydraulic fracture and weak interface is regarded as one of the main parameters affecting the fracture geometry (Lu et al., 2015). In this section, we present numerical simulations to study the effect of intersection angles on the fracture geometry. The dimensions of the model are set to be  $10 \times 10 \times 6 \text{ m}$ . The viscosity of fracturing fluid is 1 mPa s with an injection rate of  $0.005 \text{ m}^3/\text{s}$ . Note that the injection rate used in the calculations is a quarter of total injection due to the symmetry assumption. Three cases of intersection angles ( $\theta = 45^\circ, 60^\circ, 80^\circ$ ) are used. The input parameters of pay zone and barrier are listed in Table 3. Fig. 5 shows the fracture geometry for varying intersection angles. The trajectory of HF is arrested by NF for the case of low intersection angle (Fig. 5a). The crossing in conjunction with separations are observed for the case of medium intersection angle (Fig. 5b). The further increasing of the intersection angle makes the decreasing of interfacial separations (Fig. 5c). The interaction results are consistent with the plane strain models (Guo et al., 2015). Sesetty and Ghassemi (2017) presented a numerical model simulating complex fracture network in unconventional reservoirs. They found that low intersection angle NFs are mechanically closed due to the effect of stress shadow from mechanically opened parts of the fracture network. The conclusion provides new insight of fracture network stimulation. From



**Fig. 4.** Fractures geometries comparing with the experimental results (Bahorich et al., 2012), (a) HF bypass NF for the case of shorter NF, (b) HF bypass NF with one side of diverted fracture propagation for the case of taller NF, (c) geometry of the numerical model, (d) mesh scheme of the model.

**Table 3**

Input parameters of the simulation cases.

Parameters	Pay zone	Barrier	Unit
Height	1	5	m
Elastic modulus	15	20	GPa
Tensile strength of rock matrix	2	2	MPa
Permeability	10	1	mD
Vertical in-situ stress	15	15	MPa
Maximum horizontal in-situ stress	11	12	MPa
Minimum horizontal in-situ stress	8	9	MPa
Fluid leakoff coefficient (NF&HF)	$1 \times 10^{-13}$	$1 \times 10^{-14}$	m/(Pa s)
Fluid viscosity	0.001	0.001	Pa-s

Fig. 5b, the HF penetrates the NF with the opening of NF. As the aperture of HF is significantly larger than NF, the fluid flows into NF is decreased dramatically. Therefore, the opening of NF will be restricted as the HF penetrates NF. In addition, it is noted that the fracture aperture along vertical direction is not identical. In order to evaluate the ability that HF reopens cemented NFs, a scalar parameter called fracture area ratio is proposed. It is defined as the separation area of NF divided by the area of HF,  $A_{NF}/A_{HF}$ . The areas of yellow and red regions in Fig. 5d are characterized by  $A_{HF}$  and  $A_{NF}$ , respectively. When some input parameters are the same, such as the injection volume of hydraulic fluid is equal in the case of different intersection angles, the calculated  $A_{HF}$  will be approximation in the different cases. Therefore, the parameter can be used to compare the separation of NFs ( $A_{NF}$ ) of the stimulation cases. The evolution of  $A_{NF}/A_{HF}$  versus injection time for different intersection

angles is shown in Fig. 6. The  $A_{NF}/A_{HF}$  increases with the injection time for intersection of  $45^\circ$ , which implies that the fluid completely intrudes into NF without further extension in predefined HF trajectory after intersection. The HF and NF propagate simultaneously at the intersection angle of  $\theta = 60^\circ$ , while the  $A_{NF}/A_{HF}$  is smaller than the case of  $\theta = 45^\circ$ . The  $A_{NF}/A_{HF}$  is decreasing after the injection time of 1.9 s for  $\theta = 80^\circ$  due to no further extension of NF.

### 3.2. Sensitivity to in-situ stresses

The horizontal in-situ stress contrast is recognized as one of the principle factors affecting the interactions between HF and NF (Olson and Taleghani, 2009). In this section, we try to investigate the influence of vertical and horizontal in-situ stress contrast on fracture geometry. For the base case, the in-situ stresses are selected from Table 3. The varying of vertical stress contrast for different cases through increases the in-situ stresses in barrier. The intersection angle is set to be  $90^\circ$ . Fig. 7 shows the fractures geometry and  $A_{NF}/A_{HF}$  for varying vertical stress contrast. It is demonstrated that the HF is bypassing NF for the conditions of low vertical stress contrast. The  $A_{NF}/A_{HF}$  increases with the vertical stress contrast. The increment of stress in barrier confines the propagation of HF long vertical direction, which facilitates to enlarge the separations of NF. Note that the geometry of NF is changing with the vertical stress contrast. Therefore, the vertical stress contrast between pay zone and barrier has a significant effect on the separations of NF.

To further investigate the effect of stress magnitude with same vertical stress contrast on the intersections, we fix the stress in barrier, and changing vertical in-situ stress contrast by decrease stresses in pay zone.

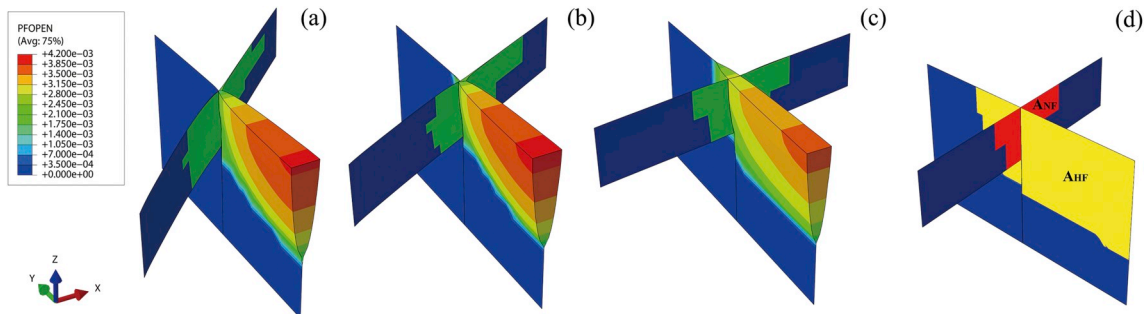


**Fig. 5.** Fractures geometry for different intersection angles  $\theta$ , (a)  $\theta = 45^\circ$ , (b)  $\theta = 60^\circ$ , (c)  $\theta = 80^\circ$ .

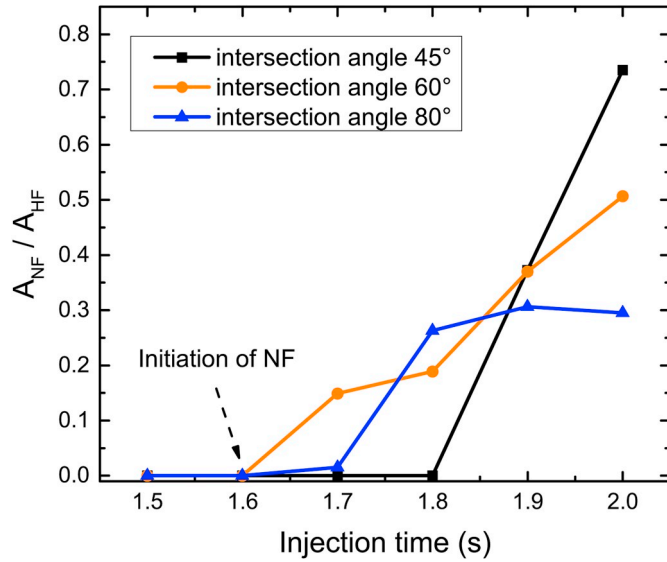


Fig. 6. Evolution of fracture area ratio for injection time.

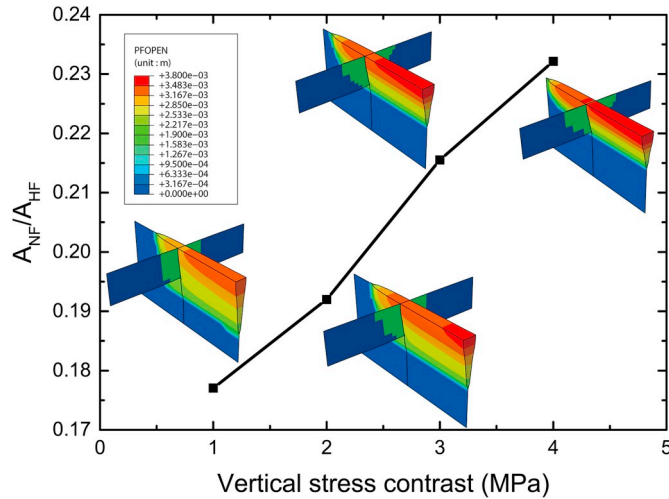


Fig. 7. Evolution of fractures geometry for varying vertical stress contrast (by changing barrier).

The minimum horizontal in-situ stress in barrier is 9 MPa. The other parameters are same with the previous models. Fig. 8 shows the fractures geometry and  $A_{NF}/A_{HF}$  for varying vertical in-situ stress contrast. The height of HF and  $A_{NF}/A_{HF}$  show a significant different from the case of same stress contrast in Fig. 7. Therefore, the magnitude of in-situ stress also affects the fractures geometry.

Four cases of calculations with different horizontal stress contrasts are presented. The vertical in-situ stress contrast between pay zone and barrier is set to be 3 MPa. The minimum horizontal stress in pay zone and barrier are set to be 8 MPa and 11 MPa, respectively. The changing of horizontal stress contrast is through increasing the maximum horizontal stress. The effect of horizontal stress contrast on the intersections is shown in Fig. 9. The vertical extent of the HF and NF is restricted to be almost the same by the stress barrier. The difference of the separation of NF is not obvious in the counter map. It is noted that the  $A_{NF}/A_{HF}$  is decreasing with the maximum horizontal stress, which indicates separated area of NF decreases with the horizontal stress contrast. The results are coincide with the conclusions posed by previous studies (Guo et al., 2015; Zou et al., 2016). However, the aperture of NF along vertical direction is not the same, indicating the effect of nonuniform distribution

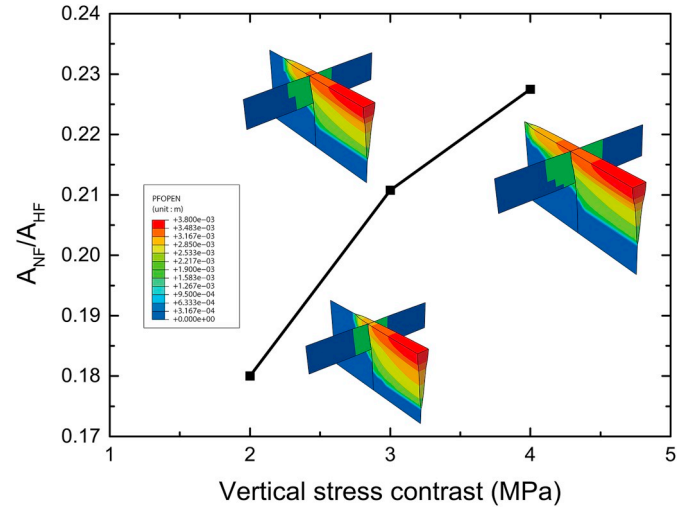


Fig. 8. Evolution of fractures geometry for varying vertical stress contrast (by changing pay zone).

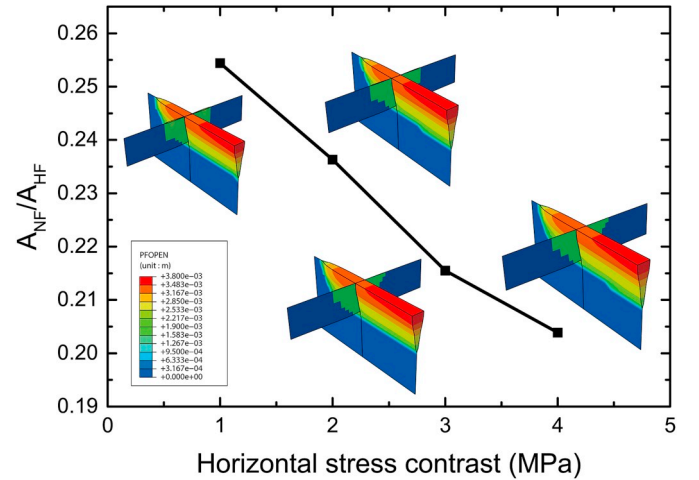


Fig. 9. Fracture geometry versus horizontal in-situ stress contrast.

of in-situ stress on fracture geometry.

To further investigate the influence of horizontal stress contrast with different vertical stress contrasts on fracture geometry. The cases of different vertical and horizontal stress contrasts are presented. In order to simplify the descriptions,  $H\cdot$  and  $V\cdot$  are used to characterize the horizontal and vertical in-situ stress contrast. H1V2 represents the horizontal and vertical stress contrast are 1 MPa and 2 MPa, respectively. The in-situ stress contrast is set to be H1V1, H3V1, H1V5 and H3V5 for the simulations. It is shown that the HF cannot open NF for the conditions of low vertical stress contrast (H1V1, H3V1 in Fig. 10). Therefore, the horizontal stress contrast has a neglected effect on fracture geometry in the cases. As the vertical stress contrast increased to 5 MPa, the extension of the fractures in vertical direction is largely restricted. The separations of NF for low horizontal stress contrast is larger than the high cases, which is consistence with the two-dimensional conclusions. The area of NF increases with the horizontal stress contrast occurs as the vertical stress contrast is large enough. Therefore, the vertical stress contrast plays an important role in reopening cemented NFs. The results of two-dimensional models are accurate when the vertical stress contrast is high enough.



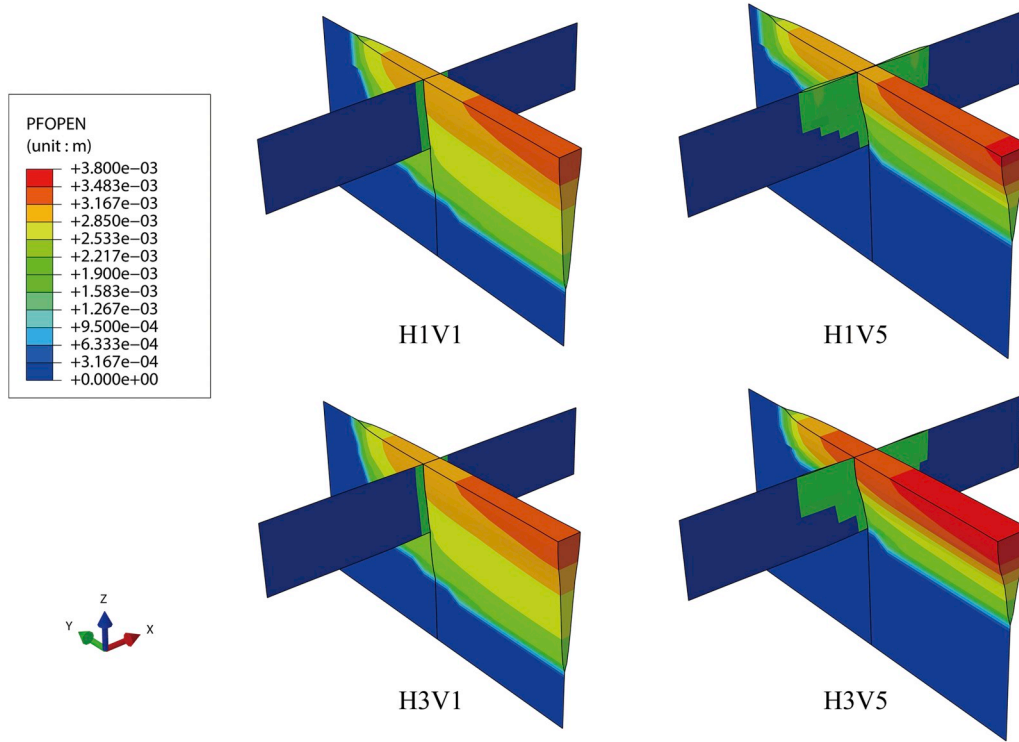


Fig. 10. Fracture geometry for different horizontal and vertical stress contrasts.

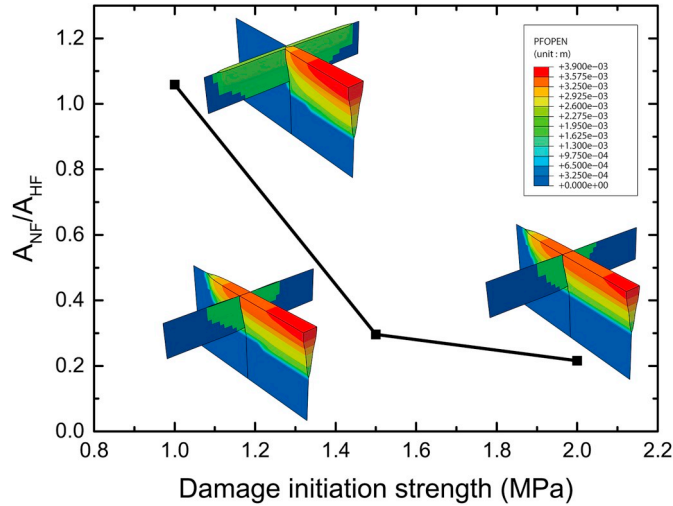


Fig. 11. Effect of rock strength on fracture geometry.

### 3.3. Sensitivity to rock strength and elastic modulus

Rock strength is varying for different reservoirs and layers. The variations of rock strength can change fractures intersection modes. Three cases of damage initiation strength in pay zone, 1 MPa, 1.5 MPa and 2 MPa are used for the studies. The intersection angle is set to be 90°. The vertical stress contrast is 3 MPa. Fig. 11 shows the influence of damage initiation strength on  $A_{NF}/A_{HF}$ . The HF is arrested by the NF for the case of low damage initiation strength. As the strength increasing, the HF is crossing NF with separation of the weak interface. The separation area of NF is decreasing with further enlarge of the strength. The fluid pressure required for the separation of fracture surfaces per area increases with the strength, while the pressure cannot be further increased significantly. Therefore, the separation area will be decreased

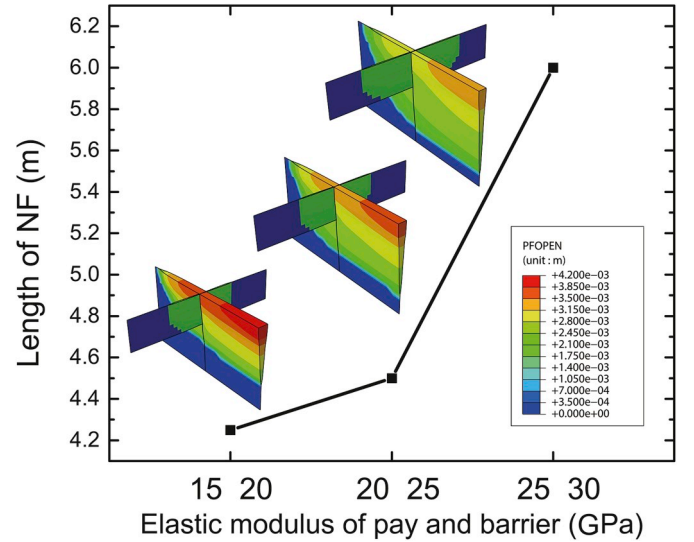


Fig. 12. Effect of elastic modulus on fracture geometry.

at the same stimulation conditions.

The brittleness of rock is regard as the one of the most important indicators for the creation of fracture network. The elastic modulus can be used to characterize the rock brittleness (Rickman et al., 2008). It is significant to conduct the effect of elastic modulus on the interactions between HF and NF. Three cases of elastic modulus of rock are investigated. The elastic modulus in pay zone and barrier, 15 GPa and 20 GPa, 20 GPa and 25 GPa, 25 GPa and 30 GPa is used. The vertical stress contrast is set to be 3 MPa. Fig. 12 illustrates the geometry of fractures intersection for varying elastic modulus. It is shown that the area of HF and NF and  $A_{NF}/A_{HF}$  increases with the elastic modulus. The increment of elastic modulus will decrease fractures aperture and facilitates to penetrate stress barrier. The fracture network is likely be created in the



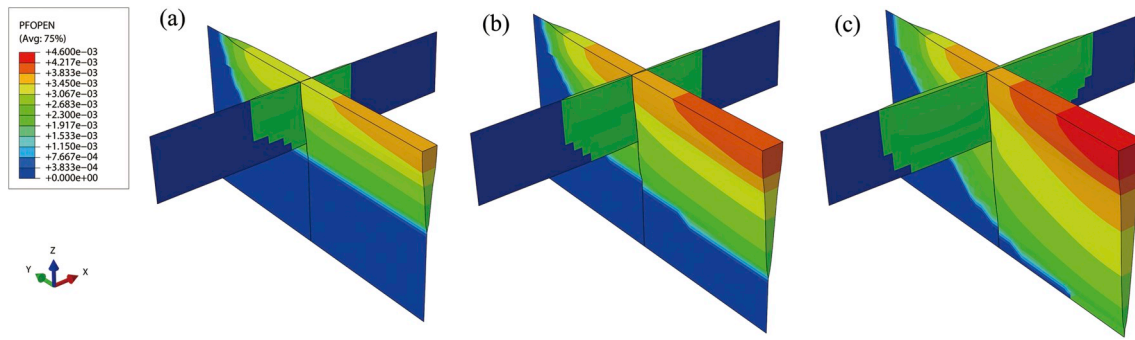


Fig. 13. Fracture geometry for varying injection rate, (a) injection rate = 0.005 m<sup>3</sup>/s, (b) injection rate = 0.01 m<sup>3</sup>/s, (c) injection rate = 0.02 m<sup>3</sup>/s.

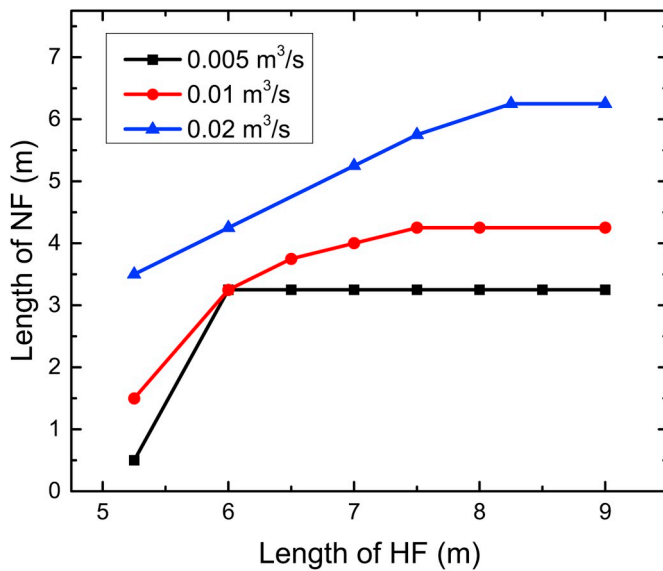


Fig. 14. Evolution of NF length versus HF length.

formation with high elastic modulus through enlarge the separation are of NF.

### 3.4. Sensitivity to injection rate

Injection rate is a significant controllable parameter of stimulation treatment. The increment of injection rate will enlarge fracture net pressure and decrease the anisotropy of horizontal in-situ stress, which facilitates to improve fracture complexity (Liu et al., 2017; Taghichian et al., 2014). In this section, three cases of injection rate, 0.005 m<sup>3</sup>/s, 0.01 m<sup>3</sup>/s and 0.02 m<sup>3</sup>/s are investigated. The other parameters are listed in Table 3. The fracture geometry of different injection rates is illustrated in Fig. 13. The increment of fluid injection rate break through the stress barrier in vertical direction. The length of NF increases with the injection rate as shown in Fig. 14. The propagation of NF is terminated at a short length of HF for the case of low injection rate. The propagation is toughness-dominated due to the small viscosity of the fluid. The shape of fractures is the function of injection rate according to the analytical solutions (Savitski and Detournay, 2002). In addition, the difference of fluid leakoff for the different injection rates also affect the fracture geometry.

### 3.5. Simultaneous fracturing with predefined NF

The opening of multiple hydraulic fractures in horizontal well will cause the stress shadow affecting the initiation and propagation of the

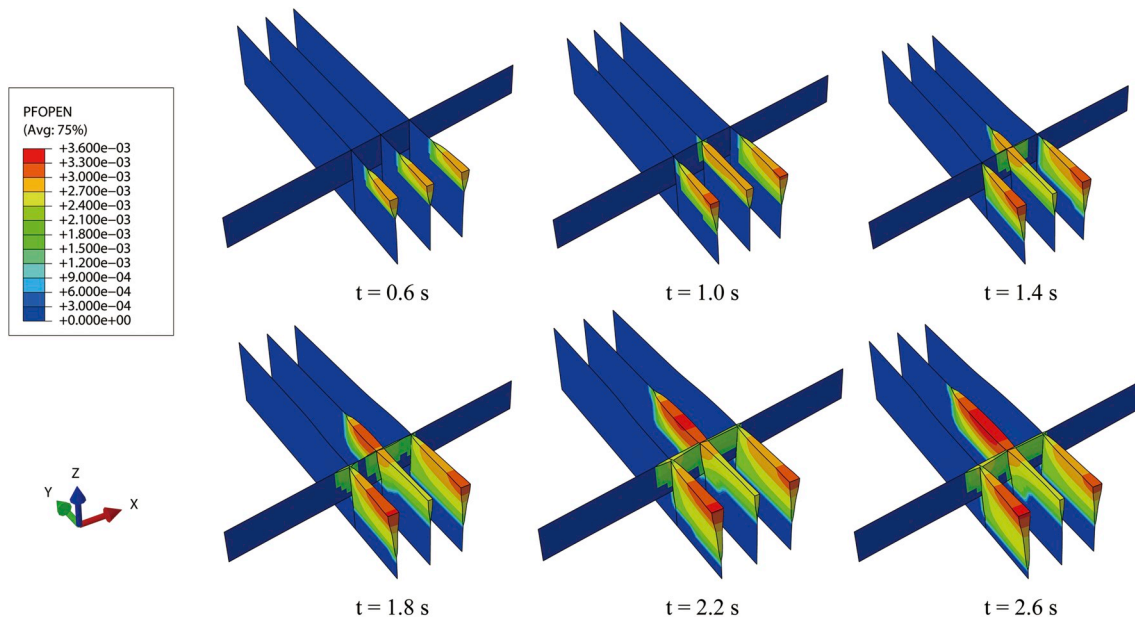


Fig. 15. Fractures intersection for simultaneous fracturing.

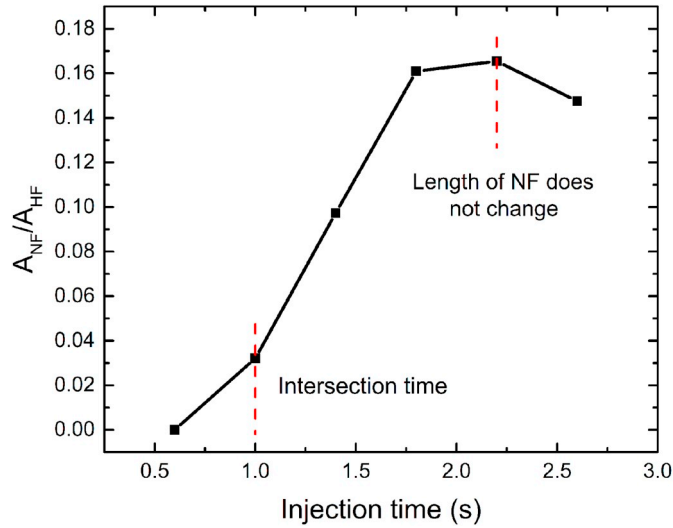


Fig. 16. Fracture area ratio versus injection time.

subsequent fractures aspects (Taghichian et al., 2014). Multiple fractures propagating simultaneously from the horizontal well is simulated in this section. The spacing of HFs is 2 m. The NF is orientated  $80^\circ$  to the maximum horizontal in-situ stress. A total injection rate of  $0.015 \text{ m}^3/\text{s}$  is used. To avoid convergence difficulties of the problem, the injection rate of different fractures is set to be uniform during stimulation process. The parameters in pay zone and barrier are listed in Table 3. The evolution of fracture geometry during stimulation treatment is shown in Fig. 15. It is shown that the stress perturbation induced by the exterior fractures restricts the propagation of HF in vertical direction. The interior fracture reaches the intersection point firstly at the injection time  $t = 1.0 \text{ s}$ . As the pumping continuing, the interior fracture penetrates the NF with a portion of separation of NF ( $t = 1.4 \text{ s}$ ). After that, the exterior HFs cannot penetrate the NF. Partial fluid is flowing into the NF, and the HFs begin propagating along vertical direction. The interior HF continues

propagating away from the horizontal well. The opening of HF will cause the increment of the minimum horizontal in-situ stress which is orientated perpendicular to the HF surface (Sneddon, 1946). The initiation and propagation of fractures are determined by the three components of nominal stress in crack tip as shown in Eq. (1). Actually, the in-situ stress perpendicular to the HF surfaces plays a dominant role on the HF initiation. When the exterior HFs reached the intersection points, the increased in-situ stress induced by the interior HF provides a restriction for further propagation of the HFs, and the fluid is pushed into other branches. The evolution of  $A_{NF}/A_{HF}$  is illustrated in Fig. 16. The length of NF does not change after the injection time of 2.25 s, and the  $A_{NF}/A_{HF}$  decreases for further injection. The opening of hydraulic fracture will cause the decreasing of horizontal stress contrast in the vicinity of the fracture. The horizontal stress contrast between HFs is less than the region of outer HFs, which facilitates to reopen the NFs between HFs.

### 3.6. Simultaneous fracturing for the conditions of different in-situ stresses

In-situ stress has a significant effect on the interactions between single HF and NF as discussed above. In this section, we conduct the simulation of simultaneous fracturing with different in-situ stresses. Four cases of in-situ stress contrast, H1V1, H1V5, H3V1 and H3V5 are simulated. The fracture geometry is shown in Fig. 17. For the cases of same horizontal stress contrast with different vertical stress contrasts (H1V1 and H1V5; H3V1 and H3V5), the separation of NF for the case of high vertical stress contrast (H1V5; H3V5) is significantly larger than the corresponding lower one. Comparing the cases of same vertical stress contrast with different horizontal stress contrasts (H1V1 and H3V1; H1V5 and H3V5), the length of NF decreases with horizontal stress contrast for the cases of higher vertical stress contrast (H1V5 and H3V5). The separation of NF is not sensitive to the horizontal stress contrast for the conditions of low vertical stress contrast. The restrictions of the vertical propagation of HFs induced by stress barrier are weakened by the complex mechanical interaction between fractures, and therefore, higher HFs are created with a small length of NF for the cases of low vertical stress contrast (H1V1, H3V1). The simulations verify that the

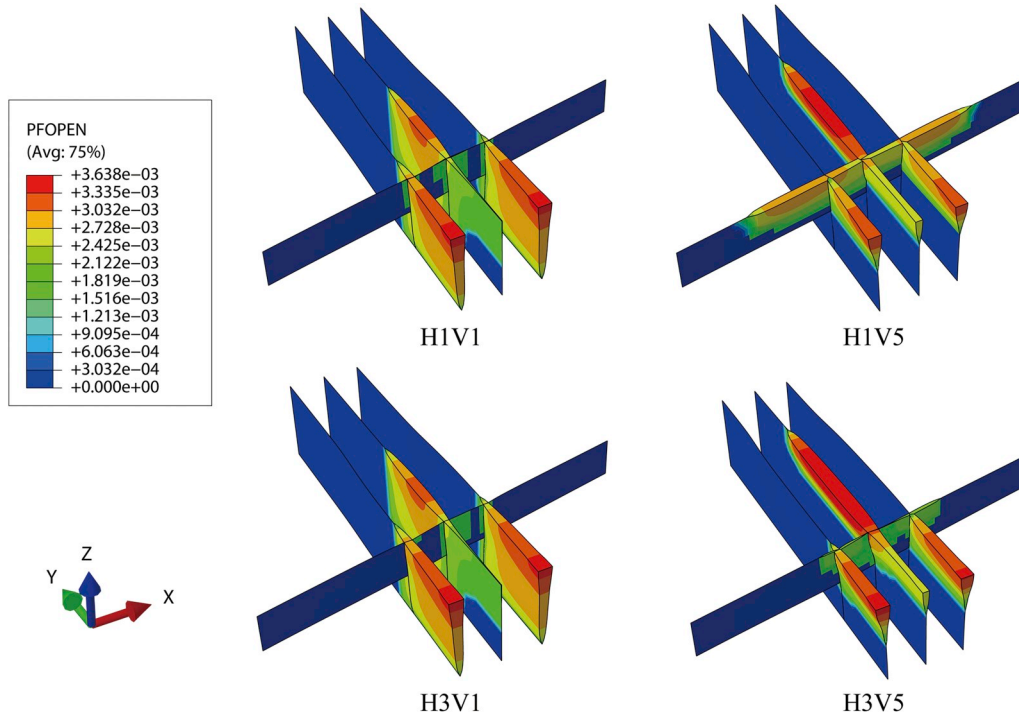


Fig. 17. Fractures geometry for varying in-situ stresses.

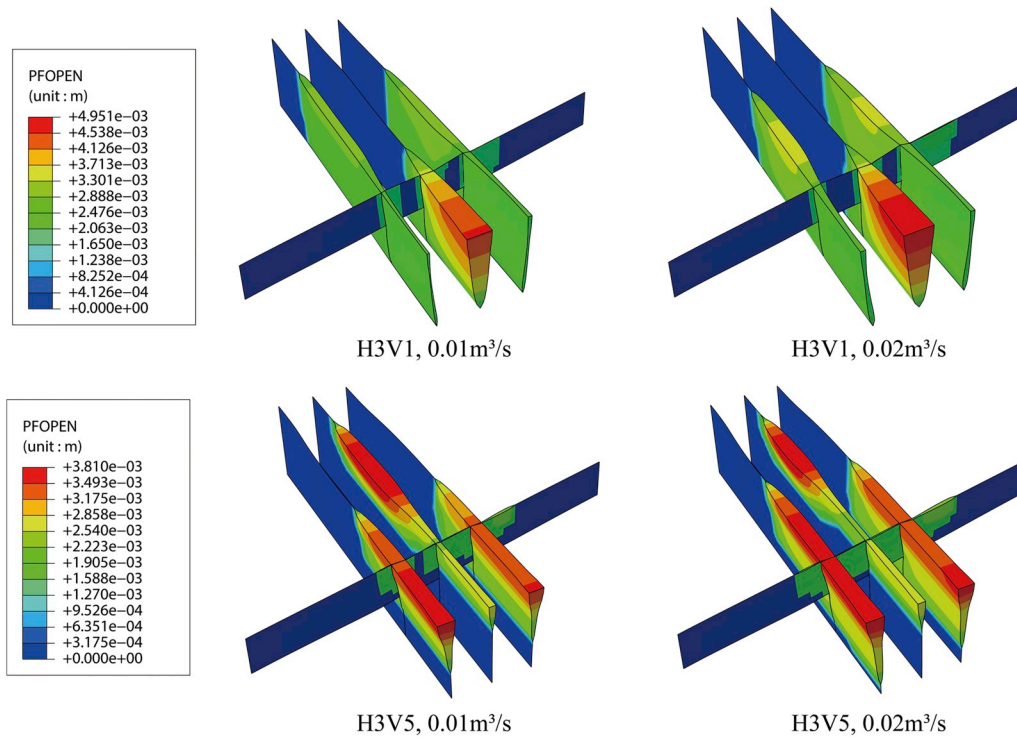


Fig. 18. Fractures geometry for varying injection rate.

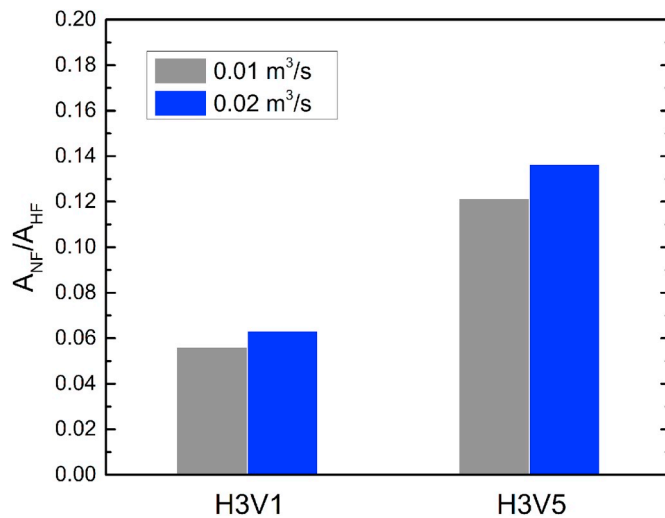


Fig. 19. Fractures area ratio for varying injection rates.

interactions between HF and NF as discussed in two-dimensional models (Fu et al., 2013; Guo et al., 2015) are applicable in the conditions of high vertical stress contrast.

### 3.7. Effect of injection rate for simultaneous fracturing

The increment of injection rate will enlarge the separation of NF for single stage fracturing as discussed in section 3.4. The effect of injection rate on the intersections between HFs and NF for simultaneous fracturing is established in this section. The injection rates used for simulations in this section are 0.01 m³/s and 0.02 m³/s, respectively. The in-situ stresses are set to be H3V1 and H3V5, respectively. Fig. 18 demonstrates the fractures trajectories for varying injection rates and stress contrasts. The propagation of HFs is jointly affected by stress shadow and the NF. The NFs and stress shadow have some effect on the

propagation of HFs, resulting nonuniform aspects of the HFs. As the injection rate increases, it become one of the controlling parameters affecting the fractures geometry, and resulting a more uniform length of HFs. The  $A_{NF}/A_{HF}$  for different injection rates is shown in Fig. 19. The separation of NF increases with the injection rate in different stress contrast conditions.

### 3.8. Effect of fracturing sequence

In this section, we investigate the effect of different fracturing methods such as simultaneous fracturing, sequential fracturing and Texas-two step fracturing on fracture geometry with predefined NF. The three fractures in the horizontal well are numbered sequentially to be Frac-1, Frac-2 & Frac-3, respectively. In simultaneous fracturing, the Frac-1, Frac-2 & Frac-3 propagate at the same time. In sequential fracturing, the Frac-1 is firstly fractured, and then the Frac-2 & Frac-3 propagate sequentially. In Texas-two step fracturing, the Frac-2 is firstly fractured, and the Frac-2 & Frac-3 propagate subsequently. Two types of stress contrast, H3V1 and H3V5, are selected for the simulations. NF is orientated 80° to the maximum horizontal in-situ stress. The fractures geometry of different fracturing sequences is illustrated in Fig. 20. For Texas-two step fracturing, due to the significant increment of in-situ stress induced by exterior HFs, the propagation of interior HF along horizontal direction is largely restricted. The interior HF break through the stress barrier, and propagates along vertical direction even in the condition of high vertical stress contrast (H3V5), which is neglected in plain strain models (Soliman et al., 2010). The nonuniform distribution of HF aperture in vertical direction increases the complexity of the mechanical interactions between HF and NF.

### 3.9. Stimulation parameters optimization to improve fracture complexity for Texas-two step method

To alleviate the severe restrictions of interior HF propagation for Texas-two step fracturing, we attempt to find out more reasonable fracturing strategies. Two NFs which is orientated 80° and 70°



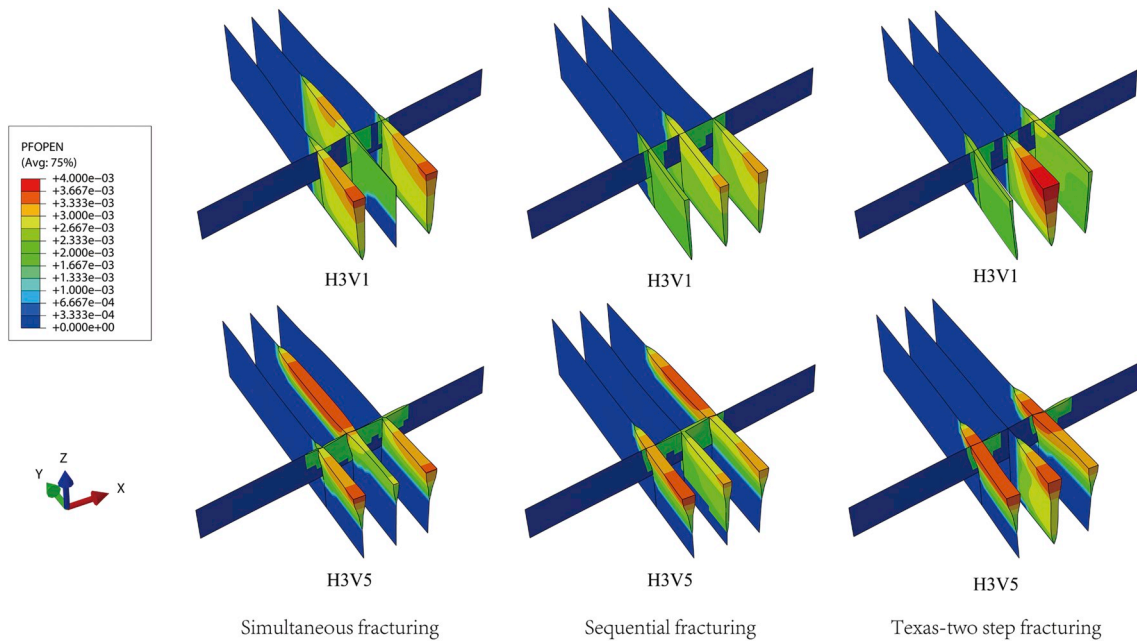


Fig. 20. Fractures geometry of different fracturing sequences.

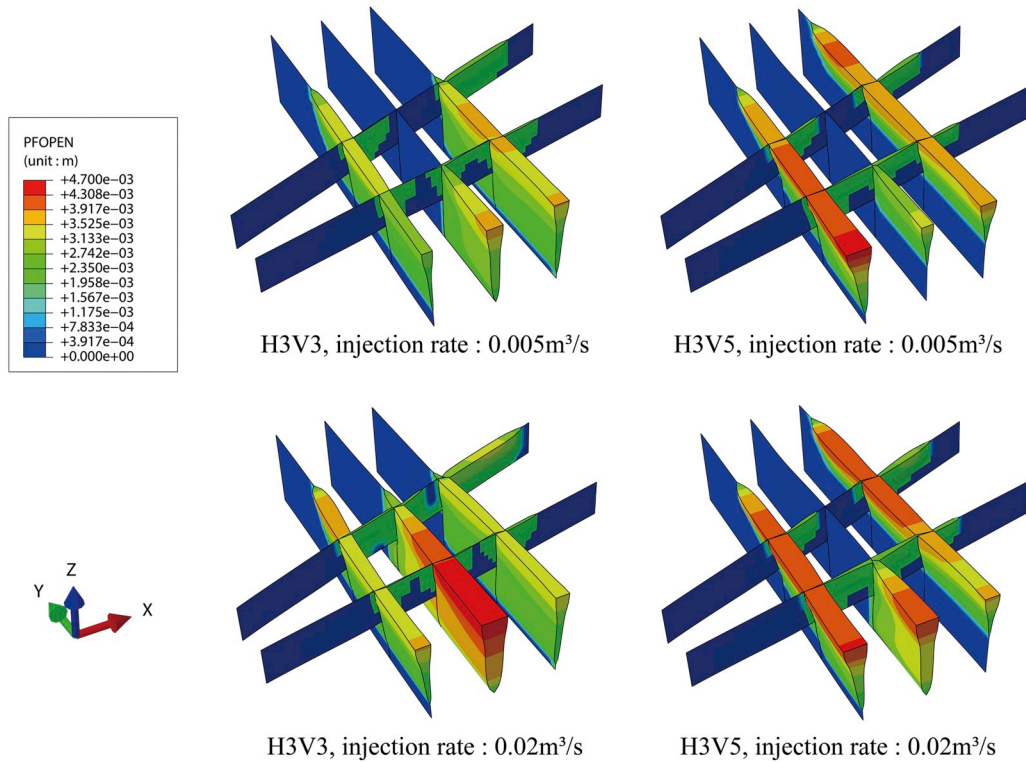


Fig. 21. Texas-two step fracturing of different injection rates.

respectively to the maximum in-situ stress are used in the simulations. Injection rates of each stage are set to be 0.005 m³/s and 0.02 m³/s, respectively. Fig. 21 shows the propagation of interior HF in horizontal direction is restricted by the stress increment caused by exterior HFs. After the separated NFs induced by different stages are connected with each other, the fluid injected into interior HF will partially flow into exterior HFs, which provides another restriction for the propagation of interior HF. When the injection rate is increased, the interior HF bypass the NFs for the case of low vertical stress contrast (H3V3), while for the

higher case (H3V5) the interior HF cannot penetrate single NF. The increment of injection rate is not an effective method driving the propagation of interior HF in horizontal direction due to the effect of stress shadow is not decreased. Therefore, the mechanical interactions between HFs should be weakened to promote the propagation of interior HF.

In order to decrease the mechanical interactions and alleviate the connection of separated NFs induced by different stages, the fracture spacing should be enlarged to be the minimum spacing that the NFs of



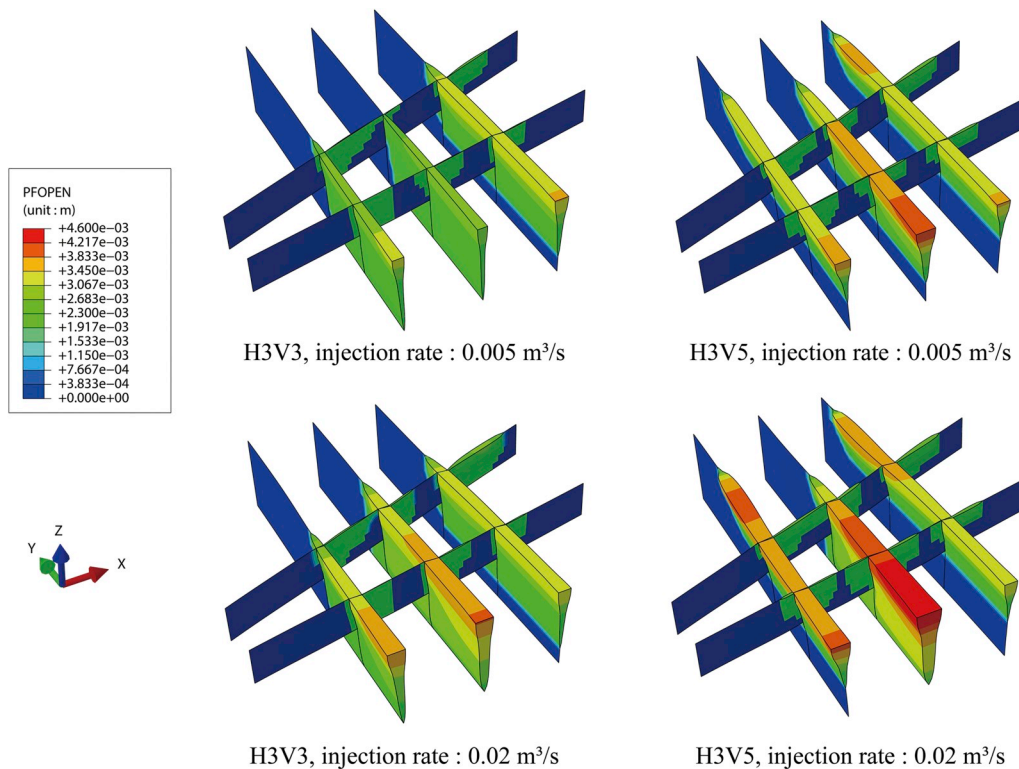


Fig. 22. Fracture geometry for varying stress contrasts and injection rates of interior HF.

different stages could connect with each other. In addition, a high injection rate should be performed in the interior HF to enlarge the separations of NFs. The optimized fracture spacing selected in this case is 4 m, and the higher injection rate of interior HF is set to be  $0.2 \text{ m}^3/\text{s}$ . The other parameters are same with above modes. The fracture geometry of different stress contrasts and injection rates are illustrated in Fig. 22. The interior HF successfully penetrates the NFs in different stress contrasts, and the separations of NFs are enlarged as a high injection rate of interior HF is performed.

#### 4. Conclusions

The fully coupled fluid-solid numerical model built in this paper incorporates the nonuniform distribution of in-situ conditions in three dimensions, such as the in-situ stress, the rock properties and NFs. The model can be used to simulate hydraulic fracturing in naturally fractured reservoirs. The effects of geologic conditions and operational parameters on the intersections between HF and NF have been performed. The vertical stress contrast is found to be a significant factor affecting the creation of fracture network in different stimulation techniques. Large separations of NFs cannot be generated in the field of low vertical stress contrast even though the horizontal in-situ stress contrast is small enough. The intersection modes predicted by the previous two-dimensional models coincide with the three-dimensional results when the vertical containment is high enough. The increment of injection rate facilitates to promote the separations of NF in varying in-situ conditions. For Texas-two step fracturing, the propagation of interior HF along horizontal direction will be restricted at the closely spaced HFs due to the severe stress shadow effect. The current study does not cover all factors that affect the interactions between HF and NF. Actually, the variations of vertical properties such as the vertical stress contrast, rock toughness and weak interfaces between layers provide similar containment of HF height growth and then the intersection modes of fractures. In addition, the presented fully coupled numerical model can be used to simulate a large number of in-situ conditions such as the arbitrary

distribution of fractures and in-situ stresses. Nevertheless, the simulation of interactions between HFs and NFs is a very complex work and many unknowns are still to be explored.

#### Declaration of competing interest

The authors declare no competing financial interest.

#### Acknowledgments

This work was jointly supported by National Natural Science Foundation of China (11525211), Anhui Provincial Natural Science Foundation (1908085QA32), the Fundamental Research Funds for the Central Universities (WK2480000003), the Natural Science Foundation of Jiangsu Province (BK20170457).

#### References

- Abaqus 6.14. Abaqus 6.14-1 Documentation.
- Bahorich, B., Olson, J.E., Holder, J., 2012. Examining the effect of cemented natural fractures on hydraulic fracture propagation in hydrostone block experiments. In: SPE Annual Technical Conference and Exhibition. Society of Petroleum Engineers.
- Batchelor, C.K., Batchelor, G.K., 2000. An Introduction to Fluid Dynamics. Cambridge university press.
- Behnia, M., Goshtasbi, K., Marji, M.F., Golshani, A., 2015. Numerical simulation of interaction between hydraulic and natural fractures in discontinuous media. *Acta Geotech.* 10, 533–546.
- Benzeggagh, M.L., Kenane, M., 1996. Measurement of mixed-mode delamination fracture toughness of unidirectional glass/epoxy composites with mixed-mode bending apparatus. *Compos. Sci. Technol.* 56, 439–449.
- Chen, Z., Jeffrey, R.G., Zhang, X., Kear, J., 2017. Finite-element simulation of a hydraulic fracture interacting with a natural fracture. *SPE J.* 22, 219–234.
- Chuprakov, D., Melchaeva, O., Prioul, R., 2014. Injection-sensitive mechanics of hydraulic fracture interaction with discontinuities. *Rock Mech. Rock Eng.* 47, 1625–1640.
- Fu, P., Johnson, S.M., Carrigan, C.R., 2013. An explicitly coupled hydro-geomechanical model for simulating hydraulic fracturing in arbitrary discrete fracture networks. *Int. J. Numer. Anal. Methods GeoMech.* 37, 2278–2300.
- Gale, J.F., Laubach, S.E., Olson, J.E., Eichhubl, P., Fall, A., 2014. Natural fractures in shale: a review and new observations. *Natural fractures in shale: a review and new observations*. AAPG Bull. 98, 2165–2216.

- Gu, H., Weng, X., 2010. Criterion for fractures crossing frictional interfaces at non-orthogonal angles. In: 44th US Rock Mechanics Symposium and 5th US-Canada Rock Mechanics Symposium. American Rock Mechanics Association.
- Gu, H., Weng, X., Lund, J.B., Mack, M.G., Ganguly, U., Suarez-Rivera, R., 2012. Hydraulic fracture crossing natural fracture at nonorthogonal angles: a criterion and its validation. *SPE Prod. Oper.* 27, 20–26.
- Guo, J., Lu, Q., Chen, H., Wang, Z., Tang, X., Chen, L., 2018. Quantitative phase field modeling of hydraulic fracture branching in heterogeneous formation under anisotropic in-situ stress. *J. Nat. Gas Sci. Eng.* 56, 455–471.
- Guo, J., Zhao, X., Zhu, H., Zhang, X., Pan, R., 2015. Numerical simulation of interaction of hydraulic fracture and natural fracture based on the cohesive zone finite element method. *J. Nat. Gas Sci. Eng.* 25, 180–188.
- Kresse, O., Weng, X., Gu, H., Wu, R., 2013. Numerical modeling of hydraulic fractures interaction in complex naturally fractured formations. *Rock Mech. Rock Eng.* 46, 555–568.
- Liu, C., Shi, F., Zhang, YongPing, Zhang, YuGuang, Deng, D., Wang, X., Liu, H., Wu, H., 2017. High injection rate stimulation for improving the fracture complexity in tight-oil sandstone reservoirs. *J. Nat. Gas Sci. Eng.* 42, 133–141.
- Lu, Y.Y., Song, C.P., Jia, Y.Z., Xia, B., Ge, Z., Tang, J., Li, Q., 2015. Analysis and numerical simulation of hydrofracture crack propagation in coal-rock bed. *CMES-Comp. Model Eng. Sci.* 105, 69–86.
- McClure, M.W., Babazadeh, M., Shiozawa, S., Huang, J., 2016. Fully coupled hydromechanical simulation of hydraulic fracturing in 3D discrete-fracture networks. *SPE J.* 21, 1–302.
- Olson, J.E., Taleghani, A.D., 2009. Modeling simultaneous growth of multiple hydraulic fractures and their interaction with natural fractures. In: *SPE Hydraulic Fracturing Technology Conference*. Society of Petroleum Engineers.
- Ortiz, M., Pandolfi, A., 1999. Finite-deformation irreversible cohesive elements for three-dimensional crack-propagation analysis. *Int. J. Numer. Methods Eng.* 44, 1267–1282.
- Renshaw, C.E., Pollard, D.D., 1995. An experimentally verified criterion for propagation across unbounded frictional interfaces in brittle, linear elastic materials. In: *International Journal of Rock Mechanics and Mining Sciences & Geomechanics Abstracts*. Elsevier, pp. 237–249.
- Rickman, R., Mullen, M.J., Petre, J.E., Grieser, W.V., Kundert, D., 2008. A practical use of shale petrophysics for stimulation design optimization: all shale plays are not clones of the Barnett Shale. In: *SPE Annual Technical Conference and Exhibition*. Society of Petroleum Engineers.
- Savitski, A.A., Detournay, E., 2002. Propagation of a penny-shaped fluid-driven fracture in an impermeable rock: asymptotic solutions. *Int. J. Solid Struct.* 39, 6311–6337.
- Sesetty, V., Ghassemi, A., 2017. Complex fracture network model for stimulation of unconventional reservoirs. In: 51st US Rock Mechanics/Geomechanics Symposium. American Rock Mechanics Association.
- Settgast, R.R., Fu, P., Walsh, S.D., White, J.A., Annavarapu, C., Ryerson, F.J., 2017. A fully coupled method for massively parallel simulation of hydraulically driven fractures in 3-dimensions. *Int. J. Numer. Anal. Methods GeoMech.* 41, 627–653.
- Shi, F., Wang, X., Liu, C., Liu, H., Wu, H., 2017. An XFEM-based method with reduction technique for modeling hydraulic fracture propagation in formations containing frictional natural fractures. *Eng. Fract. Mech.* 173, 64–90.
- Shiozawa, S., McClure, M., 2016. Simulation of proppant transport with gravitational settling and fracture closure in a three-dimensional hydraulic fracturing simulator. *J. Petrol. Sci. Eng.* 138, 298–314.
- Shrivastava, K., Agrawal, S., Kumar, A., Sharma, M.M., 2018. 3-D interactions of hydraulic fractures with natural fractures. In: *SPE International Hydraulic Fracturing Technology Conference and Exhibition*. Society of Petroleum Engineers.
- Sneddon, 1946. In: *The Distribution of Stress in the Neighbourhood of a Crack in an Elastic Solid*. Presented at the Proceedings of the Royal Society of London A: Mathematical, Physical and Engineering Sciences. The Royal Society, pp. 229–260.
- Soliman, M.Y., East, L.E., Augustine, J.R., 2010. Fracturing Design Aimed at Enhancing Fracture Complexity. Presented at the SPE EUROPEC/EAGE Annual Conference and Exhibition. Society of Petroleum Engineers.
- Sun, X., Yu, L., Rentschler, M., Wu, H., Long, R., 2019. Delamination of a rigid punch from an elastic substrate under normal and shear forces. *J. Mech. Phys. Solid.* 122, 141–160.
- Taghichian, A., Zaman, M., Devegowda, D., 2014. Stress shadow size and aperture of hydraulic fractures in unconventional shales. *J. Petrol. Sci. Eng.* 124, 209–221.
- Wang, X., Shi, F., Liu, C., Lu, D., Liu, H., Wu, H., 2018. Extended finite element simulation of fracture network propagation in formation containing frictional and cemented natural fractures. *J. Nat. Gas Sci. Eng.* 50, 309–324.
- Weng, X., Kresse, O., Chuprakov, D., Cohen, C.-E., Prioul, R., Ganguly, U., 2014. Applying complex fracture model and integrated workflow in unconventional reservoirs. *J. Petrol. Sci. Eng.* 124, 468–483.
- Yoshioka, K., Bourdin, B., 2016. A variational hydraulic fracturing model coupled to a reservoir simulator. *Int. J. Rock Mech. Min. Sci.* 88, 137–150.
- Zhang, X., Jeffrey, R.G., 2014. Role of overpressurized fluid and fluid-driven fractures in forming fracture networks. *J. Geochem. Explor.* 144, 194–207.
- Zhang, X., Jeffrey, R.G., 2006. The role of friction and secondary flaws on deflection and re-initiation of hydraulic fractures at orthogonal pre-existing fractures. *Geophys. J. Int.* 166, 1454–1465.
- Zhang, X., Jeffrey, R.G., Thiercelin, M., 2007. Deflection and propagation of fluid-driven fractures at frictional bedding interfaces: a numerical investigation. *J. Struct. Geol.* 29, 396–410.
- Zou, Y., Zhang, S., Ma, X., Zhou, T., Zeng, B., 2016. Numerical investigation of hydraulic fracture network propagation in naturally fractured shale formations. *J. Struct. Geol.* 84, 1–13.